Gold-Loaded Polymeric Micelles for Computed Tomography-Guided Radiation Therapy Treatment and Radiosensitization

Ajlan Al Zaki,[†] Daniel Joh,[‡] Zhiliang Cheng,[†] André Luís Branco De Barros,[†] Gary Kao,[‡] Jay Dorsey,[‡] and Andrew Tsourkas[†,*]

[†]Department of Bioengineering, School of Engineering and Applied Sciences, University of Pennsylvania, Philadelphia, Pennsylvania 19104, United States
[‡]Department of Radiation Oncology, Perelman School of Medicine, University of Pennsylvania, Philadelphia, Pennsylvania 19104, United States

ABSTRACT Gold nanoparticles (AuNPs) have generated interest as both imaging and therapeutic agents. AuNPs are attractive for imaging applications since they are nontoxic and provide nearly three times greater X-ray attenuation per unit weight than iodine. As therapeutic agents, AuNPs can sensitize tumor cells to ionizing radiation. To create a nanoplatform that could simultaneously exhibit long circulation times, achieve appreciable tumor accumulation, generate computed tomography (CT) image contrast, and serve as a radiosensitizer, gold-loaded polymeric micelles (GPMs) were prepared. Specifically, 1.9 nm AuNPs were encapsulated within the hydrophobic core of micelles formed with the amphiphilic diblock copolymer poly(ethylene glycol)-*b*-poly(ε-capralactone). GPMs were produced with low polydispersity and mean hydrodynamic diameters ranging from 25 to 150 nm. Following intravenous injection, GPMs provided blood pool contrast for up to 24 h and improved the delineation of tumor margins *via* CT. Thus, GPM-enhanced CT imaging was used to guide radiation therapy delivered *via* a small animal radiation research platform. In combination with the radiosensitizing capabilities of gold, tumor-bearing mice exhibited a 1.7-fold improvement in the median survival time, compared with mice receiving radiation alone. It is envisioned that translation of these capabilities to human cancer patients could guide and enhance the efficacy of radiation therapy.

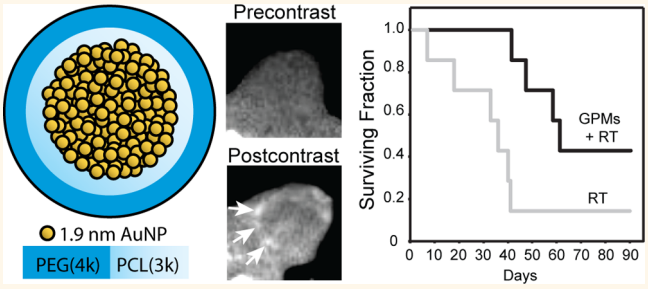

KEYWORDS: gold · nanoparticle · radiation · computed tomography · theranostic · radiosensitizer

Over the past two decades, many nanoparticle formulations have been evaluated as computed tomography (CT) contrast agents, including liposomes loaded with iodinated compounds,[1−3] polymeric iodine-containing poly(ethylene glycol) (PEG)-based micelles,[4] iodine-containing perfluorocarbons,[5,6] bismuth sulfide nanoparticles,[7] and gold nanoparticles (AuNPs).[8−10] Of these, gold nanoparticles have garnered a particularly high degree of interest. This is largely due to the high mass attenuation coefficient of gold, which is ~2.7-fold higher than iodine.[11] Accordingly, it has been found that 30 nm AuNPs can attenuate 120 kVp X-rays 5.7 times more than the iodine-based agent Ultravist.[10] Additional benefits of working with AuNPs include the ability to finely tune their size and shape and modify their surface with various functional groups. While other nanoparticle formulations, such as bismuth sulfide nanoparticles, may also exhibit higher X-ray absorption than iodine, it is difficult to control their size and there is a lack of chemical methods to modify their surface.[10,12] Surface chemistry is important when attempting to prolong systemic circulation, a prerequisite for tumor imaging and tumor accumulation *via* the enhanced permeability and retention (EPR) effect.[13] An extended circulation also offers an opportunity to image the reticuloendothelial system (RES), the blood pool, and in some cases the lymph system.

In addition to their use as CT contrast agents, AuNPs have also shown promise as radiosensitizers. Radiosensitization is due to the high absorbance of gold and the

* Address correspondence to atsourk@seas.upenn.edu.

Received for review May 7, 2013 and accepted December 30, 2013.

Published online December 30, 2013
10.1021/nn405701q

resulting deposition of energy in surrounding tissues from photoelectrons (*i.e.*, photoelectric effect), Auger electrons, and the generation of free radicals.[14,15] Within the kilovoltage energy range, the radiosensitization effect is generally attributable to the photoelectric effect, while auger electrons are hypothesized to be responsible for energy radiosensitization within the megavoltage range of radiation energies.[16−19] It has been shown that AuNPs in combination with radiation treatment can lead to an increase in the number of DNA double-strand breaks compared with radiation alone.[14,20−25] In one recent study it was shown that 1.9 nm AuNPs could even lead to an increase in the survival of tumor-bearing mice, compared with radiation therapy (RT) alone.[9] However, because of the rapid clearance of the small nanoparticles used in this study, the tumors had to be irradiated immediately after AuNP administration. In general, rapid clearance limits tumor-specific accumulation *via* EPR and, thus, can limit the ability of small AuNPs to guide, *via* CT, the precise delivery of radiation therapy.

When designing a treatment plan, radiation oncologists must take into account several critical factors including the mapping of true tumor margins, which can sometimes be challenging to define using current imaging techniques. Therefore, a more accurate definition of tumor boundaries would facilitate more precise delivery of radiation therapy and as a result decrease normal tissue exposure to undesirable radiation.[26−28] With this goal in mind, it is envisioned that long-circulating AuNPs that appreciably accumulate in tumors *via* EPR can be used to guide RT planning and treatment, through improved contrast-enhanced delineation of tumor boundaries *via* CT, thus minimizing energy deposition in surrounding healthy tissues. In addition, AuNP-mediated radiosensitization can also directly increase the radiation dose received by the tumor, thus providing a second complementary mechanism by which the overall therapeutic index can be increased.

In this study, we describe the development of a multifunctional micelle that simultaneously exhibits long circulation times, achieves appreciable tumor accumulation, generates CT image contrast, and serves as a sensitizer for radiation therapy in cellular and animal models at sublethal radiation doses. Specifically, using a microemulsion synthesis method, we have been able to prepare gold-loaded polymeric micelles (GPMs), with tunable hydrodynamic diameters ranging from 25 to 150 nm. The GPMs are formed using the amphiphilic diblock copolymer poly(ethylene glycol)-*b*-poly(ε-capralactone) (PEG-*b*-PCL) and have tightly packed clusters of 1.9 nm AuNPs incorporated within the hydrophobic core (Figure 1). We first evaluated the ability of GPMs to enhance double-stranded DNA breaks *in vitro* in response to radiation. Next, we assessed whether GPMs are capable of generating contrast for CT blood pool and tumor imaging. Finally we investigated whether the radiosensitization in cells translated to an improvement in survivability in murine tumor xenograft models.

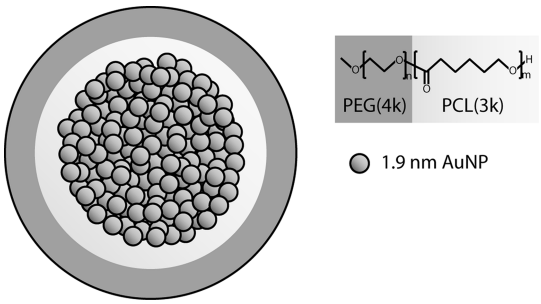

Figure 1. Schematic of gold-loaded polymeric micelles (GPMs). Gold nanoparticles are self-assembled into the hydrophobic core of micelles, stabilized with the amphiphilic diblock copolymer PEG-*b*-PCL. Each GPM is composed of approximately hundreds to thousands of individual gold nanoparticles, depending on their size.

RESULTS AND DISCUSSION

Characterization of 1.9 nm AuNPs. Hydrophobic AuNPs were prepared with dodecanethiol as a capping agent. Transmission electron microscopy (TEM) was used to characterize the mean core size of the individual hydrophobic AuNPs. TEM images showed a uniform distribution of AuNPs with a core size of 1.93 ± 0.16 nm (Supp. Figure S1). Purity was confirmed *via* UV−vis spectroscopy (Supp. Figure S2).

Synthesis and Characterization of GPMs. GPMs were prepared by encapsulating 1.9 nm AuNPs within the diblock copolymer PEG-*b*-PCL, using a microemulsion method. These GPMs were soluble in aqueous solutions owing to the hydrophilic PEG corona of the diblock copolymer. Following synthesis and purification of the GPMs, six different sizes (25−150 nm, Figure 2) were collected using differential centrifugation, as confirmed by dynamic light scattering (DLS). The DLS measurements demonstrate particle measurements with a low polydispersity index for all GPM fractions (<0.1). TEM was used to determine the morphology of the GPMs and the packing of AuNPs within the hydrophobic core. TEM micrographs revealed a narrow distribution of spherical GPMs with tightly packed clusters of AuNPs contained within the hydrophobic core of the micelles (Figure 2). The TEM micrographs also revealed a low polydispersity, correlating well with the DLS measurements. The zeta potential of the various GPM formulations was near neutral. A summary of the GPM physical-chemical properties is provided in Supp. Table S1.

Evaluation of GPMs as a Radiosensitizer. GPMs with a hydrodynamic diameter of approximately 75 nm were selected for a more detailed evaluation as radiosensitizing agents. This size was selected because it was

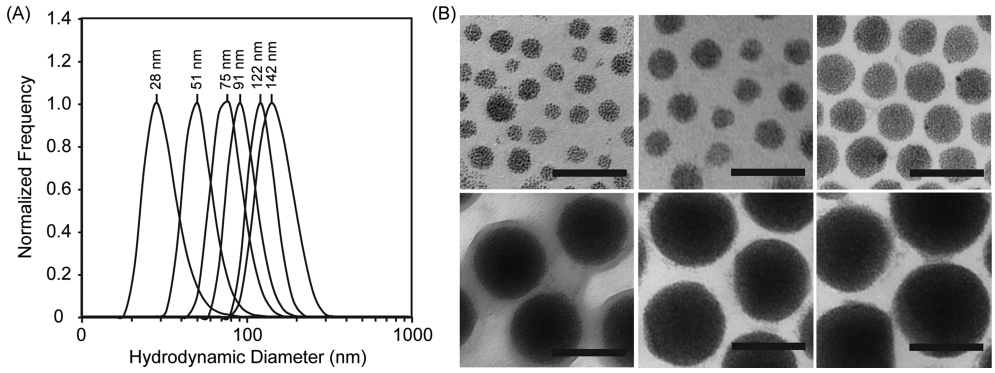

Figure 2. Size and morphology of GPMs. (A) Dynamic light scattering profiles of six GPM formulations with mean sizes ranging from 25 to 150 nm, in phosphate-buffered saline, pH 7.4. (B) Transmission electron microscopy (TEM) images of the same six GPM formulations, respectively. The electron micrographs reveal a narrow monodispersed distribution of spherical GPMs, with tightly packed gold clusters contained within the hydrophobic core (all scale bars = 100 nm).

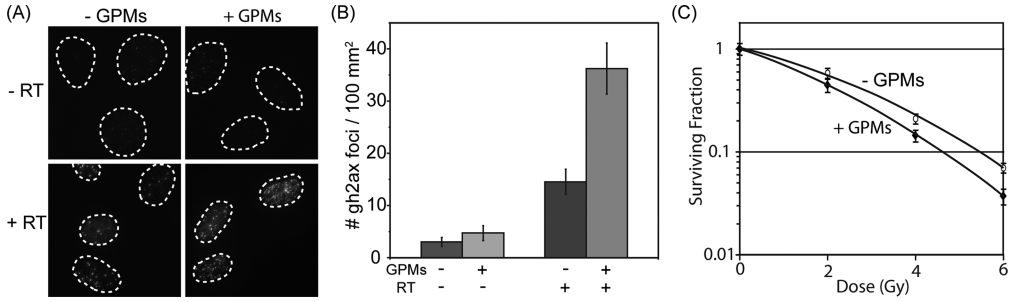

Figure 3. *In vitro* evaluation of radiation-induced DNA double-strand breaks in the presence and absence of GPMs. (A) Immunofluorescent imaging of γ-h2ax foci in HT1080 cells incubated with or without GPMs in the absence (top) or presence (bottom) of irradiation (4 Gy). (B) Quantitative analysis of γ-h2ax foci density (# foci/μm^2) for $n > 100$ cells in each treatment group. Error bars represent 95% confidence intervals. (C) Clonogenic assay of HT1080 cells treated with and without GPMs and given radiation doses of 0, 2, 4, and 6 Gy. Error bars represent the mean survival $\pm$ standard error of at least three replicates.

produced in significantly higher yields than the other sizes and was thus more amenable for *in vivo* testing. To evaluate the radiosensitization effects of the 75 nm GPMs *in vitro*, HT1080 human fibrosarcoma cells were irradiated (4 Gy) or mock irradiated in the presence or absence of GPMs and analyzed for double-strand breaks (γ-h2ax staining) (Figure 3). Immunofluorescent images revealed very low levels of γ-h2ax foci (observed as bright fluorescent spots) in unirradiated cells, regardless of the presence of GPMs. In contrast, high levels of γ-h2ax foci were observed within the nuclei of cells that received radiation treatment, with a noticeably higher number of double-strand breaks in cells that were treated in the presence GPMs. Quantitatively, there were very few γ-h2ax foci per unit area in unirradiated controls, as expected, and there was no statistically significant difference between cells incubated in the presence or absence of GPMs. However, when cells were irradiated, the number of γ-h2ax foci increased and a statistically significant difference was observed between cells irradiated in the presence and absence of GPMs ($p < 0.05$). Compared to cells receiving radiation only, the cells that were irradiated in the presence of GPMs exhibited roughly a 2.2 times higher density of DNA double-strand breaks. Furthermore, clonogenic survival assays revealed a decrease in survival of HT1080 cells irradiated in the presence of GPMs compared to those receiving irradiation alone (Figure 3). A statistically significant difference in survival ($p < 0.05$) was observed for radiation doses of 4 and 6 Gy. Using the linear-quadratic model to assess the enhancement of radiation effects, it was estimated that GPMs produced a sensitizer enhancement ratio of approximately 1.2, which is consistent with previous studies that utilized AuNPs as a radiosensitizer.[22,29]

Stability of GPMs in Serum. Prior to evaluating GPMs as an imaging and radiosensitizing agent in living subjects, the stability of 75 nm GPMs was evaluated in fetal bovine serum (Supp. Figure S3). Upon incubating the GPMs with 100% serum for 24 h at 37 °C, there was no difference in the size of the GPMs as determined by DLS, and no visible precipitates were observable in the solution. Moreover, no evidence of leaching of AuNPs from the micelle or alteration in the micelle structure was observed in TEM images following incubation in serum (Supp. Figure S4), suggesting that GPMs are sufficiently stable for *in vivo* studies. It should be noted that all of the micelle samples (*i.e.*, all size fractions) also appear to be stable in PBS at pH 7.4 for months with no observable changes in hydrodynamic diameter or structure, as determined by DLS and TEM, respectively.

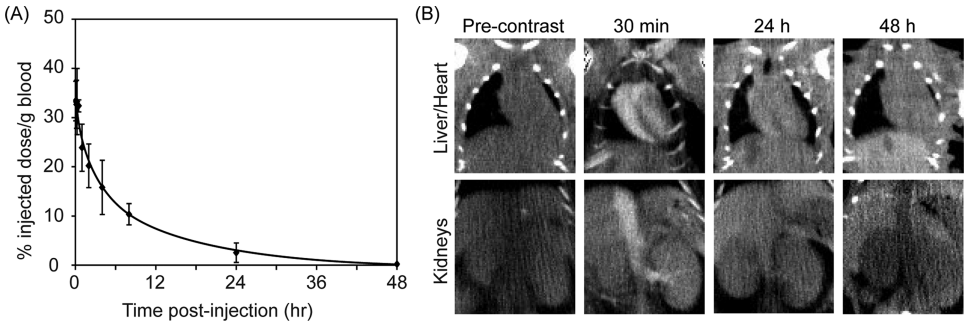

Figure 4. Blood clearance profile and CT imaging of GPMs in the blood pool. (A) ICP-OES analysis of gold content in blood at various times following the intravenous administration of GPMs to mice (n = 3). (B) Serial CT coronal views of a mouse following retro-orbital injection of 200 μL of GPM solution (650 mg/kg). Coronal views of heart and liver (top) and inferior vena cava and kidneys (bottom) are shown.

GPM Pharmacokinetics. Long circulating particles that are able to avoid rapid clearance from the bloodstream *via* glomerular filtration and the RES are necessary for EPR-driven tumor accumulation. Therefore, if GPMs are to be used to help delineate tumor margins and guide radiation therapy, it is necessary for them to exhibit a long circulation half-life. It was determined that the circulation half-life of 75 nm GPMs is ~1 h during the early distribution phase and 8.7 h during the elimination phase (Figure 4). This long circulation time is likely governed by the dense hydrophilic PEG coating present on the micelle.

The ability of GPMs to generate contrast *in vivo* was validated in mice. Images acquired 30 min postinjection demonstrated enhancement of the great vessels and minor branches such as the renal vessels and interlobular vessels (Figure 4). Furthermore, the cardiac chambers were readily visualized, demonstrating the potential use of GPMs as a blood-pool contrast agent. After 24 h there was residual enhancement of the heart and great vessels, indicative of the long circulation time of the GPMs. The administered dose of GPMs (650 mg Au/kg) was well within the range of clinically approved intravenous contrast agents. For example, iodixanol (Visipaque) is typically administered at doses ranging from 300 to 1200 mg of I/kg body weight. Additionally, the dose utilized in this study was lower than what was used in prior studies that employed gold as a radiosensitizer (*i.e.*, >1350 mg Au/kg).[9,29]

The biodistribution of GPMs was evaluated at 48 h and at 1 week postinjection by performing an inductively coupled plasma–optical emission spectroscopy (ICP-OES) analysis of gold content within the heart, kidneys, lungs, spleen, liver, feces, and urine (Supp. Table S2). As expected, the largest fractions of gold were observed in the liver and spleen. All organs examined showed a marked reduction in gold accumulation between the two time points evaluated. Specifically, ICP-OES findings revealed a 28% reduction of gold in the liver and a 47.5% reduction of gold in the spleen. Evaluation of gold content within feces and urine suggests that the primary route of clearance was biliary excretion. It is interesting to note that at the 48 h time point ~67% of the total injected dose was not accounted for in the organs analyzed or feces. It is presumed that a significant fraction of the injected gold was removed through biliary excretion within the first 24 h. Feces within the first 24 h were not collected. Upon visual inspection, no other organs appeared to exhibit any obvious signs of gold uptake, which is typically accompanied by a dark purplish hue, with the exception of the skin, which did have some discoloration.

Toxicity Analysis. The intravenous injection of GPMs (650 mg Au/kg) into healthy mice led to no signs of illness, change in activity, or weight loss (Supp. Figure S5). Notably, the amount of gold administered was well below the LD_{50}, which was previously reported to be 3.2 g Au/kg.[9] A toxicological analysis of mice 1 day and 1 week following the administration of GPMs (650 mg Au/kg) revealed normal blood chemistry, compared to saline-injected controls (Supp. Table S3).

GPMs as a CT Contrast Agent. The ability of GPMs to accumulate within tumors at sufficient levels to provide CT contrast was confirmed in mice bearing HT1080 flank tumors. Axial tumor slices of three different tumor-bearing mice were analyzed precontrast as well as 30 min, 24 h, and 48 h postcontrast (Figure 5). The variation of signal enhancement from slice to slice was accounted for by normalizing the signal to the corresponding paraspinal muscles for each slice. In the precontrast image, the tumor on the flank of the mouse located between the thigh and paraspinal muscles is not clearly delineated. At the 30 min time point, there is no qualitative or statistical difference in contrast enhancement within the tumor compared to the precontrast image. However, at 24 and 48 h postcontrast, the tumor is revealed as a hyperintense heterogeneously enhancing region with well-defined margins. These enhancements in tumor contrast were statistically different from both the precontrast and 30 min time points. This result is likely due to the

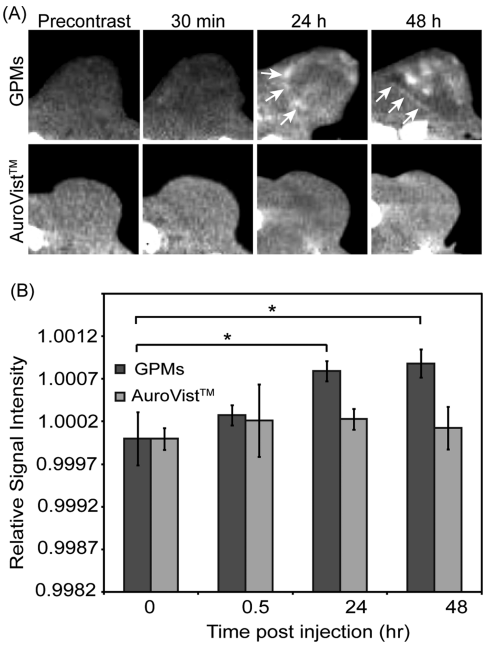

Figure 5. ***In vivo*** **CT images and intensity analysis of nu/nu nude mice with HT1080 flank tumors. (a) Representative CT images in the axial plane prior to injection (precontrast) and 30 min, 24 h, and 48 h postinjection of GPMs (*n* = 3) or AuroVist (*n* = 3). Tumor boundaries are indicated by white arrows. (b) Quantitative analysis of CT images. Signal intensity of each tumor was normalized to adjacent paraspinal muscle. For contrast measurement, the relative signal intensity was calculated as the quotient of the postcontrast to precontrast normalized tumor intensity. The asterisk indicates statistical significance (*p* < 0.05).**

extravasation of GPMs out of leaky vasculature and accumulation within the tumor owing to the EPR effect. This distinction between tumor and normal tissue can help in the design of radiation treatment of cancer by enabling visualization of regional tumor margins and spread, to help localize and maximize radiation doses to malignancies while minimizing exposure of normal tissue. Notably, within the tumor margins, the contrast enhancement was somewhat heterogeneous, likely due to variations in the ability of GPMs to penetrate far beyond the vascular wall.

To demonstrate the importance of a long circulating platform for effective extravasation and accumulation in tumors, 1.9 nm control AuNPs were also administered to tumor-bearing mice and imaged 30 min, 24 h, and 48 h postcontrast. At each time point, no visible tumor contrast enhancement was observed, compared with precontrast images. This is likely because >90% of the particles are cleared within the first 30 min.[8]

To quantitatively determine the amount of GPMs and 1.9 nm AuNPs delivered to the tumor, as well as other organs, the liver, spleen, lung, heart, kidneys, and tumor were harvested 48 h postinjection and the gold content was analyzed by ICP-OES (Figure 6). Mice injected with GPMs had the highest levels of gold in the liver and spleen and only modest levels of gold

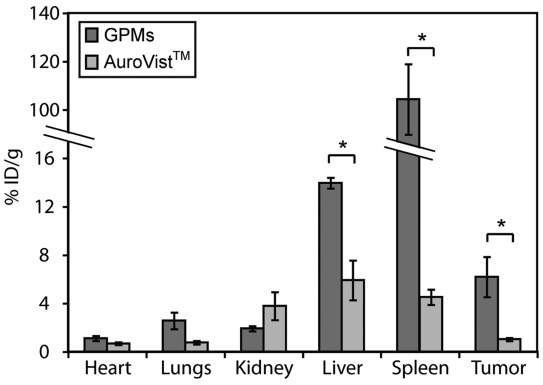

Figure 6. ICP-OES analysis of gold distribution at 48 h following the administration of GPMs or AuroVist. The percent injected dose per gram of tissue was calculated by measuring the concentration of gold in excised organs *via* ICP-OES. The asterisk indicates statistical significance (*p* < 0.05).

in the heart, lungs, and kidneys. In contrast, mice injected with 1.9 nm AuNPs had higher levels of gold within the kidney, lower uptake in the liver and spleen, and very modest uptake in the heart and lungs. This difference in organ distribution is expected since the mechanism of elimination differs for both formulations. In general neutrally charged particles with hydrodynamic sizes smaller than ~6 nm[30] are cleared from the systemic circulation *via* glomerular filtration and excreted in the urine, whereas particles greater than ~6 nm are primarily cleared by the RES system.[31] This disparity in elimination was also supported by *in vivo* CT imaging. Following GPM administration, the spleen and liver gradually brighten over the course of 48 h (Supp. Figure S6), whereas mice injected with AuroVist exhibit very bright contrast within the kidneys and bladder at early time points of CT imaging and gradually return to baseline at 24 h postinjection. With respect to tumor delivery, mice injected with GPMs displayed a statistically significant 6-fold increase in gold accumulation (6.2 ± 1.2% ID/g) compared to mice injected with AuroVist (1.0 ± 0.1% ID/g). Upon adjusting for tumor volume, the average concentration of gold within the tumor was calculated to be 0.57 ± 0.1 mg/mL and 0.14 ± 0.01 mg/mL for mice injected with GPMs and AuroVist, respectively. In general, the sensitivity for Au detection using CT imaging is estimated to be around 0.5 mg/mL.[21] However, as a result of the heterogeneous distribution of GPMs within the tumor, some regions likely have gold concentrations well above this lower detection limit. Furthermore, these tumor concentrations were well above the 0.1 mg Au/mL needed for a radiosensitization effect *in vitro*. Importantly, this circulation-mediated increase in nanoparticle delivery was sufficient to provide CT contrast prior to tumor radiation therapy. This demonstrates the importance of having a long circulating platform since the improvement in delivery has the ability to

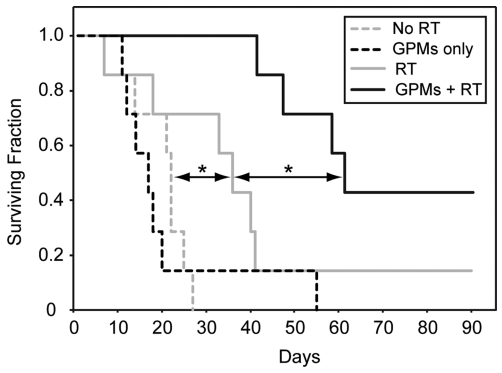

Figure 7. Kaplan–Meier survival analysis. A survival analysis was performed for tumor-bearing mice (n = 7 per group) receiving no treatment (dotted gray line), GPMs only (dotted black line), irradiation only (solid gray line), or irradiation 24 h after retro-orbital injection of GPMs (solid black line). GPMs were administered at a dose of 650 mg Au/kg. The radiation dose administered was 6 Gy at 150 kVp. The asterisk indicates statistical significance ($p < 0.05$).

yield significant contrast enhancement for CT-guided radiation therapy.

Radiosensitization of Tumors with GPMs. To specifically examine the therapeutic effects of using GPMs as radiosensitzers *in vivo*, nu/nu mice bearing 7–8 mm subcutaneous HT-1080 flank tumors were divided into four groups (n = 7 per group). The first two groups were the unirradiated controls with one of the two groups receiving GPMs. The next two groups either received radiation therapy (6 Gy) alone or were injected with GPMs 24 h prior to radiation treatment. Notably, contrast enhancement was visible within the tumors of mice receiving GPMs, which enabled CT-guided stereotactic radiation. Mice were monitored for tumor growth and were sacrificed when the tumors reached the predetermined threshold volume (1300 mm^3). The survival time was measured from the time of radiation (or mock irradiation). Mice that received GPMs prior to radiation therapy exhibited a statistically significant ($p < 0.05$) improvement in median survival (68 days), compared to mice treated with radiation alone (38 days) (Figure 7). It should be noted that all mouse groups appeared to tolerate GPMs very well over the course of study with no observable changes in behavior or symptoms of poisoning such as loss of appetite, diarrhea, or vomiting. For the group receiving radiation only, two mice were sacrificed prior to the threshold volume cutoff due to an ulcerated tumor in one and severe emaciation in another. The general observable trend in tumor growth postradiation therapy was a reduction in tumor growth, followed by a reduction in tumor volume, and then eventual tumor regrowth (Supp. Figure S7). Only one mouse out of seven in the radiation-only group, with a slow growing palpable tumor, survived 90 days post-treatment. In contrast three of the seven mice that received GPMs prior to radiation survived 90 days post-therapy. Two out of the three mice had complete remission with no palpable tumor, while the third mouse had a palpable static tumor. With respect to the unirradiated groups, GPMs alone had no effect on tumor growth compared to untreated controls. These results suggest that the EPR-dependent accumulation of GPMs within tumors can guide and enhance the efficacy of radiation therapy.

CONCLUSION

Gold nanoparticles present a promising platform for therapeutic and imaging (theranostic) applications because of their unique physical-chemical properties, their ability to be easily functionalized, and their safety profile. Gold has been used in medical practice throughout history and continues today as a treatment for rheumatoid arthritis.[32] Numerous animal studies suggest that AuNPs are also very well tolerated.[33–38] In fact, several AuNP formulations have even entered clinical trials for cancer treatment, including CYT-6091 and AuroShell. In this study 1.9 nm AuNPs were encapsulated within the biocompatible and biodegradable polymer PEG-*b*-PCL, forming gold-loaded polymeric micelles. An anticipated benefit of this GPM formulation over pegylated, solid AuNPs of similar size is that it is easy to incorporate other anticancer and/or other metallic nanoparticles into the micelle core,[39–41] if additional functionality is desirable. Moreover, we believe that the presence of many small AuNPs (1.9 nm) may allow for more rapid dissolution and excretion, compared with a single large AuNP. It was previously reported that with 40 nm solid AuNPs there is only a 9% fall in the content of gold in the liver from day 1 to 6 months.[42] In addition, many studies report inefficient clearance and a persistent accumulation of AuNPs within the reticuloendothelial system.[43–45] In contrast, we observed more than a 28% fall in gold content within the liver between day 2 and day 7. These results are very promising, although a more complete analysis must still be performed to study additional and later time points before a definitive conclusion can be drawn.

In summary, we showed that GPMs were capable of enhancing radiation-induced DNA double-strand breaks in a cell culture model, consistent with prior work with solid AuNPs.[14,15,20–25,29] Further, because of their extended clearance half-life, GPMs exhibited improved EPR-dependent accumulation in murine tumor xenografts, compared to individual 1.9 nm AuroVist nanoparticles. The higher levels of GPM accumulation in the tumor provided clear and quantifiable improvement in CT contrast. The combination of CT-guided radiation therapy and gold-mediated radiosensitization led to a statistically significant increase in the mean survival time of tumor-bearing mice compared with mice receiving radiation alone. Accurate delineation of tumor boundaries and tumor-specific radiosensitization is important for radiotherapy, due

to radiation dose limitations of the surrounding normal tissue. Therefore, we envision that GPMs can be used someday in a tractable manner to both guide and enhance the efficacy of radiation therapy.

METHODS

Synthesis of 1.9 nm Gold AuNPs. Dodecanethiol-capped AuNPs were prepared according to the procedure described by Brust *et al.*,[46] using a two-phase reduction of tetrachloroaurate ($HAuCl_4$) by sodium borohydride ($NaBH_4$) in the presence of an alkanethiol. Briefly, 30 mL of an aqueous solution of 30 mM hydrogen $HAuCl_4$ was mixed with 50 mM tetraoctylammonium bromide in 80 mL of toluene. The solution was stirred until the $HAuCl_4$ solution transferred into the organic phase. Then, 0.84 mM dodecanethiol was added to the solution while stirring followed by the dropwise addition of a 0.4 M aqueous solution of $NaBH_4$. The resultant mixture was then stirred for at least 3 h and precipitated twice at −20 °C in ethanol overnight to remove excess thiols. The precipitate was collected *via* centrifugation, and the supernatant was decanted. The remaining pellet was dissolved in toluene.

Synthesis of GPMs. Gold-loaded polymeric micelles were synthesized using oil in water emulsions and stabilized using the amphiphilic diblock copolymer polyethylene oxide (4K)−polycaprolactone (3K) (PEG-PCL). AuNPs were dissolved in toluene at 30 mg Au/mL, and PEG-PCL was also dissolved in toluene at a concentration of 50 mg/mL. A combined solution (200 μL) of the diblock (4 mg) and the AuNPs (3.5 mg) was added directly to a glass vial containing 4 mL of Millipore water, and the mixture was emulsified for approximately 3 min in an ultrasonic bath. The emulsions were then allowed to stand overnight in a desiccator prior to their characterization and purification. The resulting dark brown solution was centrifuged at 400 RCF for 10 min to remove the largest micelles. The solution was then centrifuged twice at 3100 RCF for 30 min, after which the supernatant was removed, and the pellet was resuspended in phosphate-buffered saline (PBS). Different size fractions were collected using different centrifugal rates. Free polymer and smaller sized particles were removed by diafiltration using a MidGee hoop cross-flow cartridge with a 750 kDa molecular weight cutoff (GE Healthcare, Piscataway, NJ, USA) and were then filtered through a 0.2 μm cellulose acetate membrane filter (Nalgene, Thermo Scientific) to remove any oversized particles. Finally the nanoparticles were concentrated using 50K MWCO centrifugal filter units (Millipore, Billercia, MA, USA).

Physicochemical Analysis of GPMs. GPM stock solutions were diluted in Millipore water and deposited on 200 mesh carbon-coated copper grids (Polysciences, Warrington, PA, USA) for TEM imaging using a JEOL 1010 transmission electron microscope operating at 80 kV. Stock samples of GPM were diluted in pH 7.4 phosphate-buffered saline for measuring the hydrodynamic diameter of the nanoparticles by DLS. These measurements were acquired using a Zetasizer Nano-ZS (Malvern Instruments, Worcestershire, UK) using the noninvasive backscatter mode. Zeta potential measurements were carried out by diluting GPM stock samples in pH 7.4 phosphate-buffered saline, and the mean particle zeta potential was measured using a Zetasizer Nano-ZS.

Cell Culture and γ-h2ax Immunoflourescence. HT-1080 human fibrosarcoma cells (ATCC) were cultured and maintained in Dubelcco's modified Eagle's medium, supplemented with 10% fetal bovine serum, 1% penicillin/streptomycin at 37 °C, and 5% CO_2. Cells in chamberslides were exposed to culture medium with 1 mM AuNPs for 24 h, then irradiated using a small animal radiation research platform (SARRP) (150 kVp, 15 mA). After 12 h postirradiation, cells were fixed with 10% neutral buffered formalin (Sigma-Aldrich) for 10 min. Cells were then rinsed with PBS, and the nuclei were stained with Hoechst 33342 (25 μM) for 15 min. The slides were permeabilized with 0.5% TritonX-100 in PBS and then exposed to blocking buffer (PBS, 0.5% Triton X-100, 5% normal chicken serum, 1% BSA) for 30 min at room temperature and subsequently incubated overnight at 4 °C with mouse monoclonal antiphospho-histone γ-H2AX primary antibody (JBW301, Upstate) at 1:1500 dilution in PBS (with 0.5% Triton X-100 and 1% BSA). Cells were washed with PBS and then incubated with chicken anti-mouse Alexa 594 secondary antibody (Molecular Probes) at 1:1000 dilution in PBS (with 0.5% Triton X-100 and 1% BSA) for 1 h at room temperature. After rinsing with PBS, the slides were mounted with Prolong Gold antifade reagent (Invitrogen) and coverslips. Fluorescence imaging was performed using a Deltavision Deconvolution microscope (Applied Precision) equipped with a 60× (1.42 NA) oil-immersion lens and thermoelectrically cooled 12-bit monochrome CCD camera. Images were recorded as z-stacks (0.3 μm steps). Following reconstructive deconvolution, the maximum values of the pixels were used to assemble two-dimensional projections. Foci were counted automatically using ImageJ after applying a top-hat filter and constant value threshold based on unirradiated controls.

Clonogenic Assay. Cells were incubated for 24 h in culture medium with or without 100 μg/mL of GPMs in 100 mm dishes and then irradiated with the SARRP (150 kVp, 15 mA) at the specified radiation doses (0, 2, 4, and 6 Gy). After radiation, the cells were washed three times with PBS, trypsinized, and plated at predetermined densities. The plates were kept in a humidified incubator and maintained in a 37 °C and 5% CO_2 environment for 10 to 14 days. The cells were then stained with methylene blue, and the resulting colonies counted. A colony by definition had $N > 50$ cells. The surviving fraction was calculated as (colonies counted)/(cells seeded × (plating efficiency/100)). Each point on the survival curve represents the mean surviving fraction from at least three replicates. The survival curves were fitted to a linear-quadratic equation: surviving fraction = $\exp[-(\alpha D + \beta D^2)]$. The sensitizer enhancement ratio was calculated as the ratio of the mean inactivation doses, defined as the dose at which there is 37% survival, with and without GPMs.

Quantification of Blood Clearance *via* ICP-OES. Approximately 6-week-old female nu/nu nude mice ($n = 3$) were used for the GPM blood clearance experiments. The GPMs were injected retro-orbitally at a dose of approximately 100 ppm in 200 μL of injected solution. Prior to injection, an aliquot of the GPM solution was saved for ICP-OES for the determination of the gold concentration of injected sample. Blood samples (10 μL each) were collected from each animal using the tail-nick method at 1 min, 10 min, 15 min, 30 min, 1 h, 2 h, 4 h, 8 h, 24 h, and 48 h postinjection.

Contrast-Enhanced *in Vivo* CT Imaging and Biodistribution Analysis. Approximately 6-week-old female nu/nu nude mice (Charles River Laboratory, Charles River, MS, USA) were maintained in accordance with the Insitutional Animal Care and Use Committee of the University of Pennsylvania. Mice were anesthetized using isoflurane, and HT-1080 cells were injected subcutaneously into the back left flank (2×10^6 cells in 0.1 mL of PBS). Tumors were grown until the mean diameter was approximately 7−8 mm, and precontrast cone beam CT imaging was performed using an SARRP (Gulmay Medical, Inc.). CT imaging was conducted at 50 kVp (0.5 mA), and 1440 projections were used to reconstruct the cone-beam images using the algorithm provided by the manufacturer. Immediately following the precontrast image acquisition, either GPMs or 1.9 nm AuroVist gold nanoparticles (Nanoprobes, Yaphank, NY, USA) were intravenously injected into the HT1080 tumor-bearing mice ($N = 3$ for each group). Using isoflurane to anesthetize the mice, both contrast agents were administered by retro-orbital injection (650 mg/kg Au in 0.2 mL). Postcontrast images were collected 30 min, 24 h, and 48 h postinjection with the same imaging parameters used for precontrast images. After 48 h, the animals were sacrificed and the tumors, livers, spleens, kidneys, hearts, and lungs were harvested. Tissue samples were thoroughly washed with PBS and blotted dry to minimize the contribution of any nanoparticles remaining in the bloodstream. The tissues

were weighed and digested in HNO_3 overnight at 70 °C. Following the overnight digestion, HCL was added to dissolve the gold. Samples were diluted with Millipore water and analyzed for gold content using ICP-OES.

Toxicity Studies. Twelve nude mice (female) were randomized into four groups of three animals per group receiving 650 mg Au/kg or sham-injected with phosphate-buffered saline. Animals were weighed and observed regularly for clinical signs for up to 1 week postinjection. Animals were euthanized by CO_2 1 day and 1 week after intravenous gold injections, and 0.3 mL of blood was removed from the right ventricle immediately after the cessation of breathing. Blood chemistry analytes included blood urea nitrogen, phosphate, albumin, globin, gamma-glutamyl transpeptidase, alanine aminotransferase, aspartate aminotransferase, alkaline phosphatase, total bilirubin, cholesterol, calcium, creatine, glucose, and phosphorus.

***In Vivo* Radiation Therapy.** Approximately 6-week-old female nu/nu nude mice were anesthetized using isoflurane, and HT-1080 cells were injected subcutaneously into the back left flank (2×10^6 cells in 0.1 mL of PBS). Tumors were grown until the mean diameter was approximately 7−8 mm. Next, tumor-bearing mice were split into four groups of seven each: the first group received 6 Gy RT only; the second groups received an intravenous injection of GPMs (650 mg/kg Au in 0.2 mL) 24 h prior to a single dose of 6 Gy RT; the third groups received GPMs only (*i.e.*, no RT); and the fourth group received no GPMs and no RT. When applicable, GPMs were administered by retro-orbital injection. In all groups receiving RT, CT imaging was used to localize the isocenter of the tumor. Radiation therapy was administered using a SARRP (175 kVp, 15 mA) and delivered through a 17 mm diameter collimator. Mice were monitored for tumor growth and were sacrificed when the tumor volume reached 1300 mm^3. Tumor volumes were calculated assuming an ellipsoidal tumor shape ($1/2 \times \text{length} \times \text{width}^2$).[47] Survival time to this end point was calculated from date of treatment.

Conflict of Interest: The authors declare no competing financial interest.

Acknowledgment. The authors gratefully acknowledge Dr. Cameron Koch, Walter T. Jenkins, and Lee Shuman for insightful discussions and technical support with the SARRP. This work was supported by the University of Pennsylvania Nano/Bio Interface Center (NBIC, J.D.), the Abramson Cancer Center (NCI-sponsored pilot grant, 5-P30-CA-016520-36, J.D.), NIH/NINDS (RC1 CA145075 and K08 NS076548, J.D.), NIH/NIBIB (R21 EB013754 and R21 EB013226, A.T.), American Cancer Society (IRG-78-002-33, Z.C.), and the Burroughs Wellcome Career Award for Medical Scientists (1006792, J.D.).

Supporting Information Available: Tables S1 to S3 and Figures S1 to S7. This information is available free of charge *via* the Internet at http://pubs.acs.org.

REFERENCES AND NOTES

1. Benita, S.; Poly, P. A.; Puisieux, F.; Delattre, J. Radiopaque Liposomes: Effect of Formulation Conditions on Encapsulation Efficiency. *J. Pharm. Sci.* **1984**, *73*, 1751–1755.
2. Elrod, D. B.; Partha, R.; Danila, D.; Casscells, S. W.; Conyers, J. L. An Iodinated Liposomal Computed Tomographic Contrast Agent Prepared from a Diiodophosphatidylcholine Lipid. *Nanomedicine* **2009**, *5*, 42–45.
3. Sachse, A. Iodinated Liposomes as Contrast Agents. In *Fundamental Biomedical Technologies: Nanoparticles in Biomedical Imaging*; Ferrari, M., Bulte, J. W. M., Modo, M. M. J., Eds.; Springer: New York, 2008; pp 371−410.
4. Torchilin, V. P.; Frank-Kamenetsky, M. D.; Wolf, G. L. CT Visualization of Blood Pool in Rats by Using Long-Circulating, Iodine-Containing Micelles. *Acad. Radiol.* **1999**, *6*, 61–65.
5. Long, D. M., Jr.; Lasser, E. C.; Sharts, C. M.; Multer, F. K.; Nielsen, M. Experiments with Radiopaque Perfluorocarbon Emulsions for Selective Opacification of Organs and Total Body Angiography. *Invest. Radiol.* **1980**, *15*, 242–247.
6. Patronas, N. J.; Hekmatpanah, J.; Doi, K. Brain-Tumor Imaging Using Radiopaque Perfluorocarbon - a Preliminary-Report. *J. Neurosurg.* **1983**, *58*, 650–653.
7. Rabin, O.; Perez, J. M.; Grimm, J.; Wojtkiewicz, G.; Weissleder, R. An X-Ray Computed Tomography Imaging Agent Based on Long-Circulating Bismuth Sulphide Nanoparticles. *Nat. Mater.* **2006**, *5*, 118–122.
8. Hainfeld, J. F.; Slatkin, D. N.; Focella, T. M.; Smilowitz, H. M. Gold Nanoparticles: A New X-Ray Contrast Agent. *Br. J. Radiol.* **2006**, *79*, 248–253.
9. Hainfeld, J. F.; Slatkin, D. N.; Smilowitz, H. M. The Use of Gold Nanoparticles to Enhance Radiotherapy in Mice. *Phys. Med. Biol.* **2004**, *49*, 309–315.
10. Kim, D.; Park, S.; Lee, J. H.; Jeong, Y. Y.; Jon, S. Antibiofouling Polymer-Coated Gold Nanoparticles as a Contrast Agent for *in Vivo* X-Ray Computed Tomography Imaging. *J. Am. Chem. Soc.* **2007**, *129*, 7661–7665.
11. Jackson, P. A.; Abd Rahman, W. N. W.; Wong, C. J.; Ackerly, T.; Geso, M. Potential Dependent Superiority of Gold Nanoparticles in Comparison to Iodinated Contrast Agents. *Eur. J. Radiol.* **2010**, *75*, 104–109.
12. Rabin, O.; Perez, J. M.; Grimm, J.; Wojtkiewicz, G.; Weissleder, R. An X-Ray Computed Tomography Imaging Agent Based on Long-Circulating Bismuth Sulphide Nanoparticles. *Nat. Mater.* **2006**, *5*, 118–122.
13. Peng, C.; Zheng, L.; Chen, Q.; Shen, M.; Guo, R.; Wang, H.; Cao, X.; Zhang, G.; Shi, X. Pegylated Dendrimer-Entrapped Gold Nanoparticles for *in Vivo* Blood Pool and Tumor Imaging by Computed Tomography. *Biomaterials* **2012**, *33*, 1107–1119.
14. Butterworth, K. T.; Coulter, J. A.; Jain, S.; Forker, J.; McMahon, S. J.; Schettino, G.; Prise, K. M.; Currell, F. J.; Hirst, D. G. Evaluation of Cytotoxicity and Radiation Enhancement Using 1.9 nm Gold Particles: Potential Application for Cancer Therapy. *Nanotechnology* **2010**, *21*, 295101.
15. Cheng, N. N.; Starkewolf, Z.; Davidson, R. A.; Sharmah, A.; Lee, C.; Lien, J.; Guo, T. Chemical Enhancement by Nanomaterials under X-Ray Irradiation. *J. Am. Chem. Soc.* **2012**, *134*, 1950–1953.
16. Coulter, J. A.; Hyland, W. B.; Nicol, J.; Currell, F. J. Radiosensitising Nanoparticles as Novel Cancer Therapeutics--Pipe Dream or Realistic Prospect? *Clin. Oncol.* **2013**, *25*, 593–603.
17. Dorsey, J. F.; Sun, L.; Joh, D. Y.; Witztum, A.; Al Zaki, A.; Kao, G. D.; Alonso-Basanta, M.; Avery, S.; Tsourkas, A.; Hahn, S. M. Gold Nanoparticles in Radiation Research: Potential Applications for Imaging and Radiosensitization. *Transl. Cancer Res.* **2013**, *2*, 280–291.
18. Douglass, M.; Bezak, E.; Penfold, S. Monte Carlo Investigation of the Increased Radiation Deposition Due to Gold Nanoparticles Using Kilovoltage and Megavoltage Photons in a 3D Randomized Cell Model. *Med. Phys.* **2013**, *40*, 071710.
19. Lechtman, E.; Mashouf, S.; Chattopadhyay, N.; Keller, B. M.; Lai, P.; Cai, Z.; Reilly, R. M.; Pignol, J. P. A Monte Carlo-Based Model of Gold Nanoparticle Radiosensitization Accounting for Increased Radiobiological Effectiveness. *Phys. Med. Biol.* **2013**, *58*, 3075–3087.
20. Chithrani, D. B.; Jelveh, S.; Jalali, F.; van Prooijen, M.; Allen, C.; Bristow, R. G.; Hill, R. P.; Jaffray, D. A. Gold Nanoparticles as Radiation Sensitizers in Cancer Therapy. *Radiat. Res.* **2010**, *173*, 719–728.
21. Hainfeld, J. F.; Dilmanian, F. A.; Zhong, Z.; Slatkin, D. N.; Kalef-Ezra, J. A.; Smilowitz, H. M. Gold Nanoparticles Enhance the Radiation Therapy of a Murine Squamous Cell Carcinoma. *Phys. Med. Biol.* **2010**, *55*, 3045–3059.
22. Jain, S.; Coulter, J. A.; Hounsell, A. R.; Butterworth, K. T.; McMahon, S. J.; Hyland, W. B.; Muir, M. F.; Dickson, G. R.; Prise, K. M.; Currell, F. J.; *et al.* Cell-Specific Radiosensitization by Gold Nanoparticles at Megavoltage Radiation Energies. *Int. J. Radiat. Oncol., Biol., Phys.* **2011**, *79*, 531–539.
23. Liu, C. J.; Wang, C. H.; Chen, S. T.; Chen, H. H.; Leng, W. H.; Chien, C. C.; Wang, C. L.; Kempson, I. M.; Hwu, Y.; Lai, T. C. *et al.* Enhancement of Cell Radiation Sensitivity by

Pegylated Gold Nanoparticles. *Phys. Med. Biol.* **2010**, *55*, 931–945.
24. Zhang, X. D.; Wu, D.; Shen, X.; Chen, J.; Sun, Y. M.; Liu, P. X.; Liang, X. J. Size-Dependent Radiosensitization of PEG-Coated Gold Nanoparticles for Cancer Radiation Therapy. *Biomaterials* **2012**, *33*, 6408–6419.
25. Zheng, Y.; Hunting, D. J.; Ayotte, P.; Sanche, L. Radiosensitization of DNA by Gold Nanoparticles Irradiated with High-Energy Electrons. *Radiat. Res.* **2008**, *169*, 19–27.
26. Stone, H. B.; Coleman, C. N.; Anscher, M. S.; McBride, W. H. Effects of Radiation on Normal Tissue: Consequences and Mechanisms. *Lancet Oncol.* **2003**, *4*, 529–36.
27. Engelmeier, R. L.; King, G. E. Complications of Head and Neck Radiation Therapy and Their Management. *J. Prosthet. Dent.* **1983**, *49*, 514–522.
28. Bernier, J.; Hall, E. J.; Giaccia, A. Radiation Oncology: A Century of Achievements. *Nat. Rev. Can.* **2004**, *4*, 737–747.
29. Joh, D. Y.; Sun, L.; Stangl, M.; Al Zaki, A.; Murty, S.; Santoiemma, P. P.; Davis, J. J.; Baumann, B. C.; Alonso-Basanta, M.; Bhang, D.; *et al*. Selective Targeting of Brain Tumors with Gold Nanoparticle-Induced Radiosensitization. *PLoS One* **2013**, *8*, e62425.
30. Longmire, M.; Choyke, P. L.; Kobayashi, H. Clearance Properties of Nano-Sized Particles and Molecules as Imaging Agents: Considerations and Caveats. *Nanomedicine (London)* **2008**, *3*, 703–17.
31. Choi, H. S.; Liu, W.; Misra, P.; Tanaka, E.; Zimmer, J. P.; Itty Ipe, B.; Bawendi, M. G.; Frangioni, J. V. Renal Clearance of Quantum Dots. *Nat. Biotechnol.* **2007**, *25*, 1165–1170.
32. Pricker, S. P. Medical Uses of Gold Compounds: Past, Present, and Future. *Gold Bull.* **1996**, *29*, 53–60.
33. Connor, E. E.; Mwamuka, J.; Gole, A.; Murphy, C. J.; Wyatt, M. D. Gold Nanoparticles Are Taken up by Human Cells but Do Not Cause Acute Cytotoxicity. *Small* **2005**, *1*, 325–327.
34. Lasagna-Reeves, C.; Gonzalez-Romero, D.; Barria, M. A.; Olmedo, I.; Clos, A.; Ramanujam, V. M. S.; Urayama, A.; Vergara, L.; Kogan, M. J.; Soto, C. Bioaccumulation and Toxicity of Gold Nanoparticles after Repeated Administration in Mice. *Biochem. Biophys. Res. Commun.* **2010**, *393*, 649–655.
35. Lewinski, N.; Colvin, V.; Drezek, R. Cytotoxicity of Nanoparticles. *Small* **2008**, *4*, 26–49.
36. Pan, Y.; Neuss, S.; Leifert, A.; Fischler, M.; Wen, F.; Simon, U.; Schmid, G.; Brandau, W.; Jahnen-Dechent, W. Size-Dependent Cytotoxicity of Gold Nanoparticles. *Small* **2007**, *3*, 1941–1949.
37. Shukla, R.; Bansal, V.; Chaudhary, M.; Basu, A.; Bhonde, R. R.; Sastry, M. Biocompatibility of Gold Nanoparticles and Their Endocytotic Fate inside the Cellular Compartment: A Microscopic Overview. *Langmuir* **2005**, *21*, 10644–10654.
38. Tkachenko, A. G.; Xie, H.; Coleman, D.; Glomm, W.; Ryan, J.; Anderson, M. F.; Franzen, S.; Feldheim, D. L. Multifunctional Gold Nanoparticle-Peptide Complexes for Nuclear Targeting. *J. Am. Chem. Soc.* **2003**, *125*, 4700–4701.
39. Torchilin, V. P. Peg-Based Micelles as Carriers of Contrast Agents for Different Imaging Modalities. *Adv. Drug Delivery Rev.* **2002**, *54*, 235–252.
40. Ai, H.; Flask, C.; Weinberg, B.; Shuai, X.; Pagel, M. D.; Farrell, D.; Duerk, J.; Gao, J. M. Magnetite-Loaded Polymeric Micelles as Ultrasensitive Magnetic-Resonance Probes. *Adv. Mater.* **2005**, *17*, 1949–1952.
41. Nasongkla, N.; Bey, E.; Ren, J.; Ai, H.; Khemtong, C.; Guthi, J. S.; Chin, S. F.; Sherry, A. D.; Boothman, D. A.; Gao, J. Multifunctional Polymeric Micelles as Cancer-Targeted, MRI-Ultrasensitive Drug Delivery Systems. *Nano Lett.* **2006**, *6*, 2427–2430.
42. Sadauskas, E.; Danscher, G.; Stoltenberg, M.; Vogel, U.; Larsen, A.; Wallin, H. Protracted Elimination of Gold Nanoparticles from Mouse Liver. *Nanomedicine* **2009**, *5*, 162.
43. Balasubramanian, S. K.; Jittiwat, J.; Manikandan, J.; Ong, C. N.; Yu, L. E.; Ong, W. Y. Biodistribution of Gold Nanoparticles and Gene Expression Changes in the Liver and Spleen after Intravenous Administration in Rats. *Biomaterials* **2010**, *31*, 2034–2042.
44. Cho, W. S.; Cho, M.; Jeong, J.; Choi, M.; Cho, H. Y.; Han, B. S.; Kim, S. H.; Kim, H. O.; Lim, Y. T.; Chung, B. H. Acute Toxicity and Pharmacokinetics of 13 nm-Sized PEG-Coated Gold Nanoparticles. *Toxicol. Appl. Pharmacol.* **2009**, *236*, 16–24.
45. Niidome, T.; Yamagata, M.; Okamoto, Y.; Akiyama, Y.; Takahashi, H.; Kawano, T.; Katayama, Y.; Niidome, Y. PEG-Modified Gold Nanorods with a Stealth Character for *in Vivo* Applications. *J Controlled Release* **2006**, *114*, 343–347.
46. Brust, M.; Walker, M.; Bethell, D.; Schiffrin, D. J.; Whyman, R. Synthesis of Thiol-Derivatized Gold Nanoparticles in a 2-Phase Liquid-Liquid System. *J. Chem. Soc., Chem. Commun.* **1994**, *7*, 801–802.
47. Tomayko, M. M.; Reynolds, C. P. Determination of Subcutaneous Tumor Size in Athymic (Nude) Mice. *Cancer Chemother. Pharmacol.* **1989**, *24*, 148–154.